

BACHELOR

Surface reactions during atomic layer deposition of cobalt phosphate

Raaijmakers, S.H.L.

Award date:
2019

[Link to publication](#)

Disclaimer

This document contains a student thesis (bachelor's or master's), as authored by a student at Eindhoven University of Technology. Student theses are made available in the TU/e repository upon obtaining the required degree. The grade received is not published on the document as presented in the repository. The required complexity or quality of research of student theses may vary by program, and the required minimum study period may vary in duration.

General rights

Copyright and moral rights for the publications made accessible in the public portal are retained by the authors and/or other copyright owners and it is a condition of accessing publications that users recognise and abide by the legal requirements associated with these rights.

- Users may download and print one copy of any publication from the public portal for the purpose of private study or research.
- You may not further distribute the material or use it for any profit-making activity or commercial gain

Plasma & Materials Processing

3CBX0

**SURFACE REACTIONS DURING ATOMIC LAYER
DEPOSITION OF COBALT PHOSPHATE**

Sander Raaijmakers 0958938

Supervisors: Dr. M. Creatore
M. Sc. V. Di Palma

Abstract

A quadrupole mass spectrometry (QMS) study has been performed on the atomic layer deposition (ALD) of cobalt phosphate (CoPi). Two CoPi ALD recipes were run and analyzed by measuring the deposition in time with a quadrupole mass analyzer (QMA). For each recipe, measurements of different mass-to-charge (m/z) ratios were done. The results were plotted and compared to the measurement results of the same recipes but without either plasma or precursor dosing. The measurements show a combustion reaction happening during the first oxygen plasma. They also show a combustion reaction happening during the second oxygen plasma, revealing a possible reaction mechanism for the burning of the ligands of trimethyl phosphate (TMP). TMP was observed to be adsorbing to the substrate surface, saturating after the third dosing. No reaction mechanisms for the adsorption of TMP on the cobalt oxide (CoO_x) surface were able to be confirmed.

Contents

Abstract	I
Abbreviations	III
1 Introduction	1
1.1 Renewable energy	1
1.2 Hydrogen production	1
1.3 Atomic layer deposition	2
1.4 Outline of the report	3
2 Theoretical background	4
2.1 Atomic layer deposition	4
2.1.1 Different ALD cycles	4
2.1.2 Thermal and plasma-assisted ALD	4
2.2 Quadrupole mass spectrometry	5
2.2.1 Qualitative description of the basic operating principle	5
3 Experimental setup	7
3.1 ALD setup and deposition process	7
3.2 In situ measurement	7
4 Preliminary testing	9
4.1 Literature research	9
4.2 Results	9
5 Results and discussion	11
5.1 Cobalt reactions	11
5.2 TMP reactions	12
5.2.1 Surface adsorption of TMP	12
5.2.2 Reaction mechanisms of TMP	13
5.2.3 Burning of the ligands of TMP	13
6 Conclusion	16
7 Acknowledgments	17
References	18
Appendix A Preliminary Testing Figures	22

Abbreviations

AC	Alternating current.
ALD	Atomic layer deposition.
Ar	Argon.
Co	Cobalt.
CoCp₂	Bis(cyclopentadienyl)cobalt(II).
CoO_x	Cobalt oxide.
CoPi	Cobalt phosphate.
DC	Direct current.
DMMP	Dimethyl methylphosphonate.
FTIR	Fourier transformed infrared spectroscopy.
GPC	Growth per cycle.
HCOOH	Formic acid.
HER	Hydrogen evolution reaction.
HOCH₃	Methanol.
IC	Integrated circuits.
Ir	Iridium.
m/z	Mass-to-charge.
OER	Oxygen evolution reaction.
OH	Hydroxyl.
P	Phosphate.
PA-ALD	Plasma-assisted ALD.
QMA	Quadrupole mass analyzer.
QMS	Quadrupole mass spectrometry.
Ru	Ruthenium.
SE	Spectroscopic ellipsometry.
STWS	Solar thermochemical water splitting.
TFC	Total final consumption.
TMP	Trimethyl phosphate.

1 Introduction

1.1 Renewable energy

With the worlds total final consumption (TFC) of energy expected to keep growing with about 1% each year for the coming two decades[1], and the known finitude of fossil fuels and their effect on climate change, increasing the share of renewable energy in the TFC is essential. One problem with renewable energy sources is that they are inconsistent throughout the day; e.g. the wind speed dictates the energy output of wind farms. This means the energy supply and demand mismatch throughout the day. When renewable energy supply is lower than the demand, additional energy has to be provided by burning fossil fuels. When renewable energy supply is higher than demand, the oversupply is wasted.

In order to address this issue, it is possible to store excess renewable energy, and then use that stored energy when there is a shortage. This energy can be stored in different ways, one of which is in the form of fuels like hydrogen[2]. Figure 1.1 shows that liquid hydrogen has an energy density of 8 MJ kg^{-1} [3], which is higher than the energy density of 0.67 MJ kg^{-1} of lithium-ion batteries[4]. Highly compressed hydrogen can also be transported over long distances relatively easily[5, 6], making hydrogen storage a viable option for solving mismatching energy supply and demand.

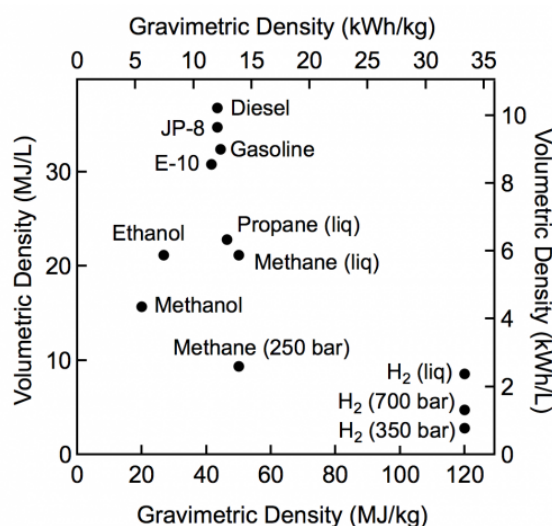


Figure 1.1: Volumetric and gravimetric energy density of different fuels[3].

1.2 Hydrogen production

One possible method to produce hydrogen is water splitting. This can be done in several ways with the use of solar or other renewable energy. One example is solar thermochemical water splitting (STWS), which gets its thermal energy from solar energy[7]. This technique is based on the dissociation of water in a single step, direct thermolysis, which is unlikely to become feasible in the near future due to the high temperature requirements ($>2000 \text{ K}$) needed to separate H_2 and O_2 [7, 8]. Two-step STWS is a promising technique where a metal oxide is first heated to produce O_2 , and then reoxidized by exposing it to H_2O , producing H_2 [9, 10, 11]. However, the temperatures required are still high ($>1000 \text{ K}$)[9, 7], limiting the possible applications of this technique. Another way to split water is water electrolysis, also known as electrochemical water splitting. Water electrolysis uses a cathode for the hydrogen evolution reaction (HER) and an anode for the oxygen evolution reaction (OER)[12]. At the anode, water is split into oxygen, hydrogen ions, and electrons; as seen in equation (1.1)[12, 13]. At the cathode, ionized hydrogen is combined with electrons to create hydrogen; as seen in equation (1.2)[12, 14]. Combining these half-reactions gives the full reaction, which can be seen in equation (1.3).





The theoretical minimum potential required for this reaction is 1.23 eV[12, 15, 16]. However, due to the complexity and slow speed of the OER, an overpotential is required[12, 17, 13]. The higher the overpotential, the lower the usable voltage, and thus the lower the efficiency of the process.

To solve this problem and make the process more efficient, nano-structured electrocatalysts are used. These catalysts are introduced at the water-electrode interface and are able to lower the overpotential needed[12]. The approximate current density expected from a solar-water splitting device is 10 mA cm^{-2} , and while several catalysts for the HER are known that could operate at this current density with an overpotential of $<0.1 \text{ eV}$, lowering the overpotential of the OER has proven to be a harder problem to solve[18, 17, 18]. At the moment, the most promising materials for the OER are iridium (Ir) and ruthenium (Ru); which are capable of lowering the overpotential to 400 meV at current densities of 10 mA cm^{-2} , as can be seen in Figure 1.2[12]. However, these noble materials are expensive and rare[19, 20]. Because of this, lots of research is done to find other materials that are less expensive.

Promising alternatives are cobalt (Co)-based catalysts, as can also be seen in Figure 1.2. In the past years, several types of Co-based catalysts like sulfide [21], nitride [22], and phosphate (P) [23] have been studied. CoPi has been acknowledged for its catalytic activity in neutral environments, and its long-term electrochemical stability[23]. As the ratio of Co/P is important for the activity of CoPi, it is preferable to be able to control the composition at an atomic level[24]. One possible way to achieve this level of control is with ALD.

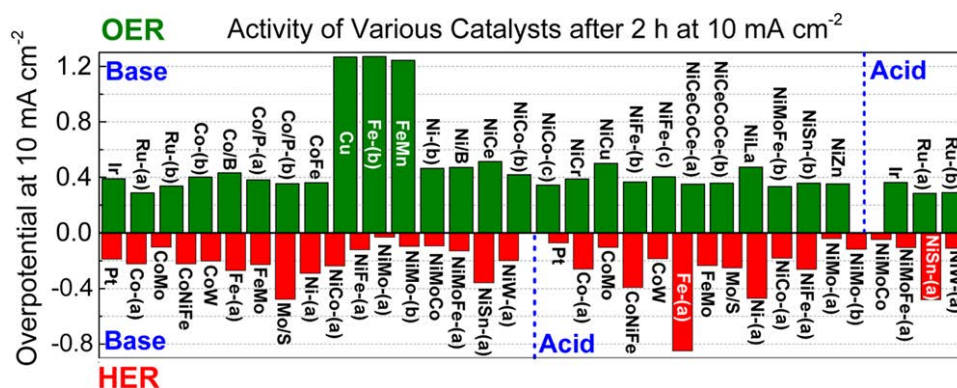


Figure 1.2: Overpotential of different materials for the HER and OER[18].

1.3 Atomic layer deposition

ALD is a thin-film deposition technique based on the sequential dosing of a gas or vapor phase precursor[25]. For ALD, this precursor typically is an inorganic coordination compound; which is a metallic center, surrounded by bound molecules called ligands. A co-reactant, often a small molecule like O_2 , N_2 , etc., is also used during a typical ALD cycle[26].

The advantages of ALD over more conventional deposition methods are the precise growth control, and the conformality and uniformity of the deposited layers. A representation of these characteristics within a surface can be seen in Figure 1.3. Due to the self-limiting nature of the surface reactions during ALD, growth can be controlled at the monolayer level[25]. For these reasons, interest in ALD has been rising quickly since the 1990s, especially for the production of silicon-based microelectronics[27]. As integrated circuits (IC) are being made with increasing aspect ratios and decreasing film thickness, ALD has attracted attention in the IC industry as well[28]. Some other applications of ALD are nanotechnology[29], electronic and optoelectronic materials[30], and catalysts[31].

Because of the good control of material properties possible with ALD, it is a good candidate for the production of CoPi electrocatalysts, as mentioned in section 1.2. Currently, CoPi is grown mainly through (photo)electrodeposition

in solution, which means control of the growth is influenced by current, electrolytes, and PH[32, 33]. More precise control of the exact composition of the CoPi, with a different Co/P ratio, is expected to result in better water splitting efficiency[24].

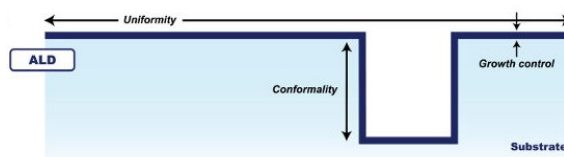


Figure 1.3: Visual representation of conformality, uniformity, and growth control on a substrate[34].

The ALD process described by V. Di Palma et al.[24] is one way of growing CoPi. Every ALD cycle consists of four steps: first dosing of bis(cyclopentadienyl)cobalt(II) (CoCp_2); second oxygen plasma; third dosing of TMP; and fourth one more oxygen plasma step. While this ALD recipe is known to work for growing CoPi, little is known about the reactions happening at the surface. This is a common occurrence with ALD processes, where an ALD process is already in use for practical applications, while the exact physicochemical reactions are still unknown[35]. Studying this aspect of the ALD process gives an insight into what is actually happening during film growth.

To gain more insight into these reactions, this study will focus on looking at what is happening at the surface during this ALD process by looking at different molecules that are present in the reaction chamber. This will be done by using QMS to look at possible reaction byproducts and TMP ions during the TMP dosing step. Using this, conclusions can be drawn about what is happening at the surface, gaining a better understanding of the deposition process. This knowledge could then be used to make hydrogen production more efficient, which can be used to make the transition to renewable energy easier.

1.4 Outline of the report

First, in section 2, the theoretical background of ALD and QMS will be discussed. In section 3 the details of the setup used for the preliminary and final experiments are given. The next two sections, section 4 and 5, present and discuss the results of the preliminary and final experiments. Finally, a conclusion will be drawn from these results in section 6.

2 Theoretical background

2.1 Atomic layer deposition

As already mentioned in section 1.3, ALD is a thin film deposition technique, ideal for depositing layers of solid material with a high conformality, uniformity, and control of thickness. ALD relies on the self-limiting nature of the reactions happening on the substrate surface. For a reaction to be self-limiting, the precursor and co-reactant should only be able to react with available surface sites, and not with themselves, or the surface groups that they create[26]. If these conditions are true, the precursor reacts with the substrate until it is saturated, and then stops reacting completely.

2.1.1 Different ALD cycles

Most ALD processes consist of two reactants, creating a binary reaction sequence[25]. In this case, the total ALD cycle consists of four steps. First reactant A is dosed. The dosing time is long enough to saturate the substrate. This creates a single layer of reactant A on the substrate surface. The second step is a purging step. In this step, the reaction products that are created during the surface reaction, together with the excess precursor, are pumped away. It is necessary to pump these molecules away to avoid a reaction between reactant A and B in the gas phase or on the surface, which can lead to impurities in the deposited material. The third step is the dosing of reactant B, also to saturation. Lastly, another purging step pumps away all products in the reaction chamber[26]. This process repeats itself x times in an $(AB)_x$ sequence and is depicted in Figure 2.1.

There are also other, more advanced, ALD cycles, consisting of more than two reactants. One example is a multistep ALD cycle, which could have three reactants, dosed in an $(ABC)_x$ sequence with a purging step in between. Another possibility is an ALD supercycle. A supercycle could, for example, combine two regular binary ALD cycles to form one supercycle by dosing in an $[(AB)_x(CD)_y]$ sequence. These more advanced ALD cycles open the possibility to create tertiary and quaternary compounds like $SrTiO_3$ and $InSn_xO_y$ [26], together with CoPi, which is researched in this study.

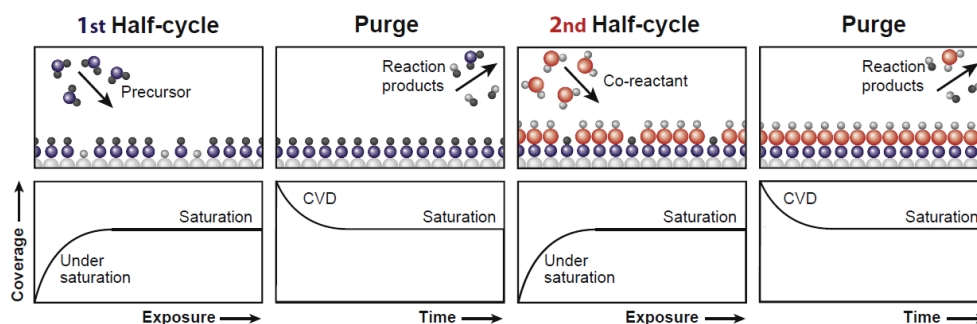


Figure 2.1: Schematic representation of a binary ALD cycle[26].

2.1.2 Thermal and plasma-assisted ALD

Most binary ALD cycles are done using thermal ALD. These reactions happen at various temperatures and are referred to as thermal ALD because they can take place without the assistance of plasma[25]. The basic ALD cycle described in section 2.1.1 is an example of thermal ALD.

Plasma-assisted ALD (PA-ALD) uses a plasma source to generate radicals; for instance hydrogen radicals. These radicals are able to remove ligands from the reactant on the surface like described in the following reaction scheme[25]:





where $*$ denotes a surface species and \cdot denotes a radical. This way single element ALD materials can be grown, and it is also useful for growing materials at lower temperatures. Low temperature PA-ALD enables the growth of materials that would be impossible to grow using thermal ALD. An example of this is the reaction in equation (2.2), where the hydrogen molecules are not reactive enough to reduce the Ta precursor using thermal ALD, needing temperatures as high as 400°C [36].

The ALD cycle researched in this study also uses PA-ALD but with oxygen radicals instead of hydrogen radicals. This is necessary to remove the ligands from the CoCp_2 after the Co dosing step.

2.2 Quadrupole mass spectrometry

QMS is done using a QMA. This analyzer consists of four parallel, cylindrical rods. While the rods would ideally have a hyperbolic cross-section, most rods in actual QMAs are cylindrical, because of practical and economical reasons[37]. Between each opposing pair of rods, a voltage is applied. This gives the analyzer the ability to filter ions with a specific m/z ratio from a gas[38]. An example of a QMA can be seen in Figure 2.2. Because QMA's resolve ions based on their m/z ratio instead of their momentum or kinetic energy, unit mass resolution is preserved even for populations with broad velocity distributions[37]. By also avoiding the use of magnets, the cost, bulk, and weight can be kept low. This makes the QMA a popular device for making mass spectra, and adaptations are even used in space flight and real-time environmental monitoring[39, 40].

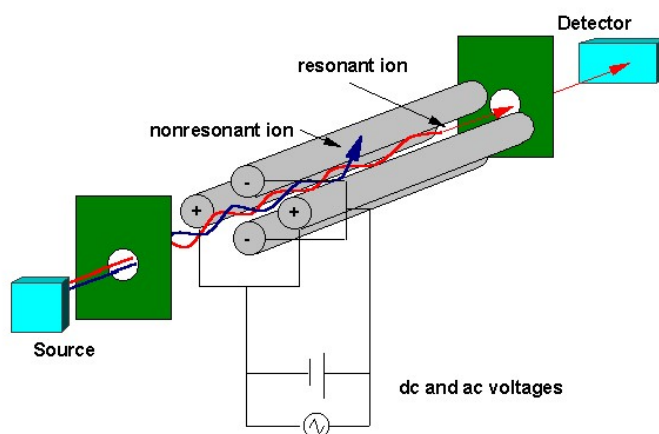


Figure 2.2: Schematic of a QMA[38].

2.2.1 Qualitative description of the basic operating principle

To filter ions with only a specific m/z ratio, different potentials are applied between the two sets of opposing rods, which are essentially electrodes. Two of them have an applied potential of $(U + V \cos(\omega t))$, and the other two have an applied potential of $-(U + V \cos(\omega t))$, where U is a direct current (DC), $V \cos(\omega t)$ an alternating current (AC), t the time, and ω [38] the angular frequency of the applied waveform.

The electrodes spend half a cycle at a positive potential and half a cycle at a negative potential. When this potential is positive, positive ions will be accelerated towards the center. When the potential is negative, positive ions will be accelerated towards the electrodes. The effect the potential has on an ion is higher when the m/z ratio of the ion is lower. A positive DC potential is applied between two of the electrodes. Ions with a larger m/z ratio tend to be less affected by the AC potential, and more by the average, positive, DC potential. This means they stay mostly in the center between the two electrodes. However, ions with a lower m/z ratio will be more affected by the AC potential, and when sufficiently light, the acceleration during the negative potential causes

the particle to collide with the electrodes. The ion is then discharged and pumped away. This means the two electrodes with a positive DC potential work as a low pass filter[37].

The other two electrodes have a negative DC potential. This means that the ions with a larger m/z ratio, that tend to be more affected by the negative DC potential than by the AC potential, are now drifting outwards towards the electrodes. When they reach the electrodes they are also discharged and pumped away. This means the two electrodes with a negative DC potential work as a high pass filter[37].

Combined these four electrodes can ensure only ions with a specific m/z ratio are able to remain inside the QMA and reach the detector without being discharged.

3 Experimental setup

3.1 ALD setup and deposition process

CoPi films were deposited using a home-built ALD machine as described in more detail by Y. Hajar et al.[41], H.C.M. Knoops et al.[42], and S.B.S. Heil et al.[43]. In short, this setup consists of an inductively coupled plasma source, connected to a deposition chamber, connected to a turbo pump that can reach a base pressure of 10^{-6} mbar. The temperature of the substrate holder was set to $300\text{ }^{\circ}\text{C}$ and the temperature of the walls of the reaction chamber was set to $100\text{ }^{\circ}\text{C}$. CoCp_2 and TMP (purity 97%) were used as precursors and both were purchased from Sigma-Aldrich. Argon (Ar) (purity $>99.999\%$; base pressure $2.2 \cdot 10^{-2}$ mbar) was used as a carrier gas for the dosing of CoCp_2 . As reactant, an oxygen plasma ($8.0 \cdot 10^{-3}$ mbar; 100 W) was used. The CoCp_2 was contained in a stainless steel bubbler held at a temperature of $80\text{ }^{\circ}\text{C}$, which was connected to the reaction chamber with a line held at $100\text{ }^{\circ}\text{C}$. The TMP was vapor-drawn from a stainless steel TMP bubbler with a temperature of $50\text{ }^{\circ}\text{C}$, through a line held at $70\text{ }^{\circ}\text{C}$, to the deposition chamber. An overview of the setup can be found in Figure 3.1.

As the goal of this study is to find the surface reactions of TMP on CoO_x , a fitting ALD cycle had to be designed. To do this, preliminary tests were done. From these tests, two final experiments were designed.

In the first experiment, an ALD cycle for CoPi deposition was run with first 4 s of CoCp_2 dosing, then 10 s of oxygen plasma, then 1.2 s of TMP dosing, and lastly 4 s of oxygen plasma. This recipe is shown in Figure 3.2 as recipe 1. After each step, a purging step of 15 s was inserted to make sure all of the excess products in the chamber were gone before the next step. This recipe was repeated 300 times to make sure the pressure in the chamber is stabilized. Then this recipe was run again; once without turning on the plasma, and once without dosing the precursors. Instead of the plasma and the precursors, a delay of the exact same length was introduced.

In the second experiment, an adjusted ALD recipe for CoPi deposition was run, which is shown in Figure 3.2. The first two steps were exactly the same as before, but the TMP dosing step was repeated three times. After this, the second oxygen plasma step is also repeated three times. This recipe was also run without the CoCp_2 dosing step, instead introducing a delay of the same length.

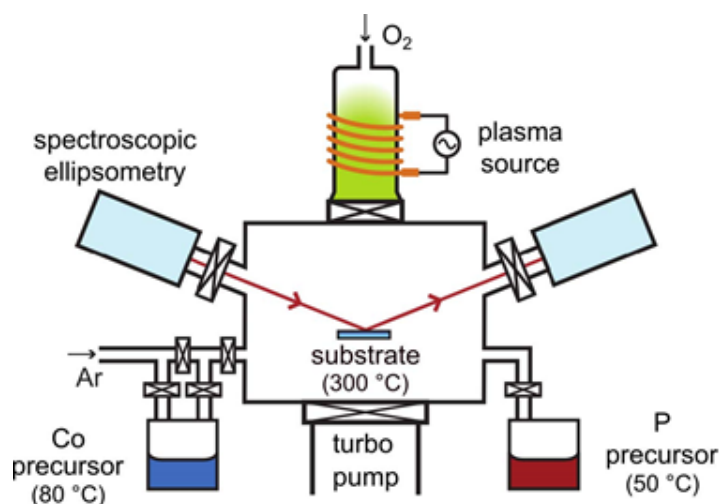


Figure 3.1: A schematic overview of the ALD reactor setup[44].

3.2 In situ measurement

QMA was used to measure the reaction by-products and other molecules present in the reaction chamber. The spectrometer used was the QME 200 from Pfeiffer and was attached to the top of the reaction chamber. This spectrometer can measure ions with an m/z ratio of 1-100 and has an electron ionizing energy of 70 eV. The

¹Visual representation based on the dosing scheme figure in the article of V. Di Palma et al[24].

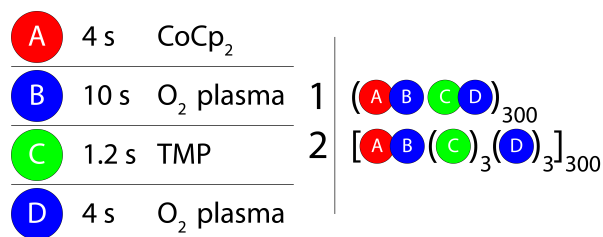


Figure 3.2: Scheme with the dosing time of each step (left) and the two recipes used (right).¹

area of the chamber walls is considerably larger than the area of the substrate, meaning a part of the measured signal of byproducts can originate from reactions on the chamber walls.

The m/z ratios chosen to follow were different during both recipes and chosen after the preliminary testing. The reason that they are different is that the first recipe was mainly used to analyze steps A, B, and D; while the second recipe was used to analyze step C. The reasons for this are discussed in section 4.2. The m/z ratios and their corresponding possible ions are given in Table 3.1.

To keep track of the growth per cycle (GPC) during the ALD process, in situ spectroscopic ellipsometry (SE) was done with a J.A. Woollam, Inc. M2000U (0.75-5.0 eV) ellipsometer. This was necessary to see if CoPi growth could also take place without using oxygen plasma after TMP dosing.

Table 3.1: Table of all measured m/z ratios and their corresponding ions.

	m/z	12	15	28	29	30	31	32
	Ions	C ⁺	CH ₃ ⁺	CO ⁺	OCH ⁺	OCH ₂ ⁺	OCH ₃ ⁺	O ₂ ⁺ or HOCH ₃ ⁺
Recipe number				x	x	x		x
Recipe 1				x	x	x		x
Recipe 2		x	x	x			x	x
	m/z	40	44	47	64	79	95	
	Ions	Ar ⁺	CO ₂ ⁺	PO ⁺	C ₅ H ₄ ⁺	PO ₃ ⁺ or PO ₂ CH ₄ ⁺	PO ₃ CH ₄ ⁺	
Recipe number				x	x			
Recipe 1		x	x	x	x			
Recipe 2		x	x	x		x	x	

4 Preliminary testing

To design the final experiments, preliminary testing on TMP had to be done. First, literature research into the mass spectrum of TMP was done to find the expected peaks. Following this, measurements with the QMS were done by dosing TMP into the reaction chamber and measuring the whole m/z range (10-100). After this, specific m/z ratios were chosen to be followed in time in the final experiments.

4.1 Literature research

Electron impact ionization spectra of TMP have been researched in different papers, and are also available in some spectral databases. As can be seen in Figure 4.1, the main peaks are expected around an m/z of 110, 109, 95, 79, and 80. Some smaller peaks can be seen around 47, 28, and 15. Most of these are confirmed by experiments done by Donald A. Bafus et al.[45], who also show the possible ions that are responsible for these peaks. A paper by Brunengraber et al. also gives the ionization spectrum of TMP for m/z ratios from 70 to 160. The results from Donald A. Bafus et al.[45] and Brunengraber et al.[46] can be found in Appendix A. The QMA used for the experiments in this report is not able to measure m/z ratios higher than 100. Therefore, the highest peak at an m/z of 110 is not reported.

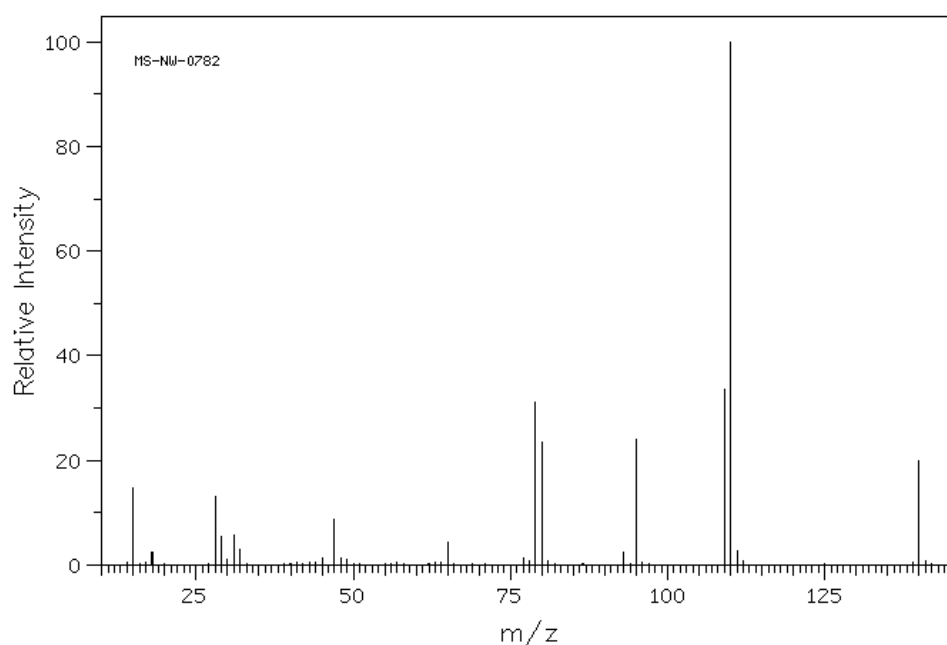


Figure 4.1: Ionization spectrum of TMP[47].

4.2 Results

First, almost the whole m/z range was measured, from 20-100. TMP was dosed multiple times without purging of the reaction chamber between the steps. Ions are expected to only have a single charge, making the m/z ratio the same as their mass. After one dosing, no clear peaks are visible around the expected m/z ratios and background noise is indistinguishable from the peaks. More dosings were done, and after dosing three times, peaks begin to emerge. Large peaks are visible in Figure A.2a around m/z ratios of 28 (CO), 40 (Ar), and 44 (CO₂). These peaks could originate from Ar and CO₂ that was still left in the chamber from dosing steps before the dosing of TMP. Expected peaks in the higher range of the m/z spectrum are also visible. When zoomed in on this region, like in Figure 4.2, the expected peaks around 79 and 80, and 95 can be seen, as well as a small peak around 63. Another peak around 94 or 93 is visible, possibly originating from the same ion as 95 (PO₃CH₄⁺), but with one or two hydrogen atoms respectively removed. Selective measurements in the range of 60-68, 76-84, and 92-100 were done to get a measurement of these regions with a better resolution. The results of these measurements and of

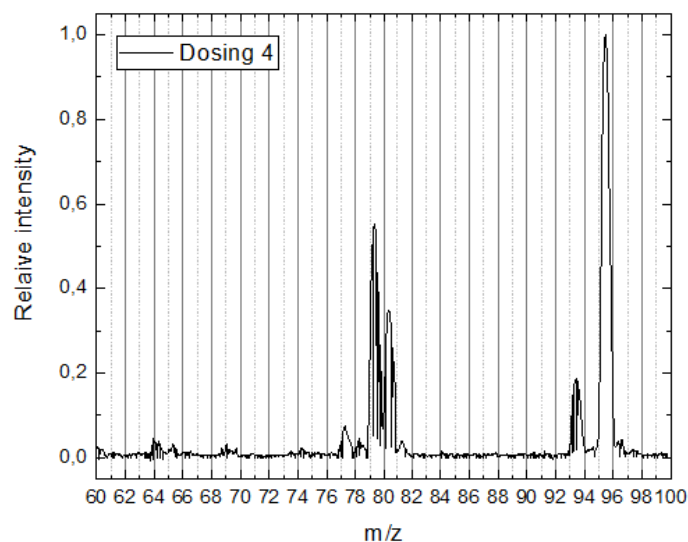


Figure 4.2: Linear plot of the electron impact ionization spectrum of TMP (m/z from 60-100).

the whole spectrum can be found in Appendix A. For all these results the background signal is subtracted from the measurements.

Because the peaks are only visible after three, longer, dosings of TMP, the base recipe mentioned in V. Di Palma et al.[24] is changed to double timings, as already mentioned in section 3.1. Also, two recipes are used: one full ALD cycle and one ALD cycle with step C and step D repeated three times. For the second recipe, QMS measurement is only done during the TMP dosing. The rest of the cycle the valve to the QMA is closed.

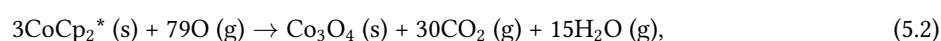
Another issue is the background noise, which is still clearly visible in-between the peaks. To reduce this background noise a longer measuring time can be used, which makes the measurement more smooth. The drawback of a longer measuring time is that the time needed to measure multiple masses increases too. This means that when multiple masses are followed in time, the composition of the gas in the reaction chamber could change before all masses have been measured. Multiple tests were done to find the optimal measuring time, and eventually a time of 50 ms was chosen.

The peaks with an m/z of 95 and 79 are the most visible ions of TMP and those were chosen to be followed for the second recipe, the triple TMP dosing. Together with these Ar was followed as a reference signal, and methanol (HOCH_3) with an m/z of 32 was followed to be able to confirm if the reaction mechanism proposed by Mitchell et al.[48], as mentioned in section 5.2.2, is happening. For the first recipe products related to the oxygen plasma and Co dosing step were followed. As mentioned in section 5.2.3, OCH_2^+ is expected to be released during the oxygen plasma. To be able to confirm this proposed reaction, the masses of OCH_2^+ and OCH^+ (29 and 30 respectively) were followed. An overview of the followed ions can be found in Table 3.1.

5 Results and discussion

5.1 Cobalt reactions

The results of the time-resolved measurements of masses 28 and 44 can be seen in Figure 5.1 and 5.2 respectively. These are the results of step A and B of the first recipe. An increase is visible for both masses during the full ALD cycle while the oxygen plasma is turned on. This indicates a combustion reaction is taking place during step B, resulting in an increase in the signal of CO_2 , which in turn also results in an increase in signal from CO, as CO_2 disintegrates in the QMA. This is in agreement with results from M.E. Donders et al.[49] on ALD of Co_3O_4 thin films. They measured a similar rise in signal from CO_2^+ and CO^+ and suggest the following reaction mechanism[49]:



where a * again denotes a surface species. This gives an indication of the combustion reaction happening at the surface, but the steps in-between are still unknown. To understand these steps better, following masses like 58 ($\text{C}_2\text{H}_2\text{O}_2^+$), 65 (Cp), and 71 ($\text{C}_3\text{H}_3\text{O}_2^+$) in future measurements might be useful, as these are possible fragments of the Cp ligands of CoCp_2 .

Another peak is visible around the 20 s mark in Figure 5.2. This could indicate a possible reaction happening. However, the peak is also visible during the cycle without plasma, in which case the substrate should not be growing and reactions are not expected. Upon closer inspection, a similar peak around the 20 s mark is visible in Figure 5.3, a measurement of Ar, which is non-reactive. This suggests the increase in signal is due to a pressure increase. The pressure increase can be explained by the switching of the Ar flow from flowing through the bubbler to flowing directly into the chamber, causing a possible increase in pressure.

To account for the influence of pressure increases in future measurements, a non-reactive gas can be flowed through the reaction chamber at a constant speed. This signal can be used as a reference signal, making it possible to distinguish pressure changes from an increase of a certain ion. This would make it possible to verify if the peaks observed around 20 s in Figure 5.1 and 5.2 are truly from a pressure increase. It would also help in confirming if the first peak in Figure 5.4, as mentioned in section 5.2, is a result of the valve to the QMA opening, or if it is the result of something else.

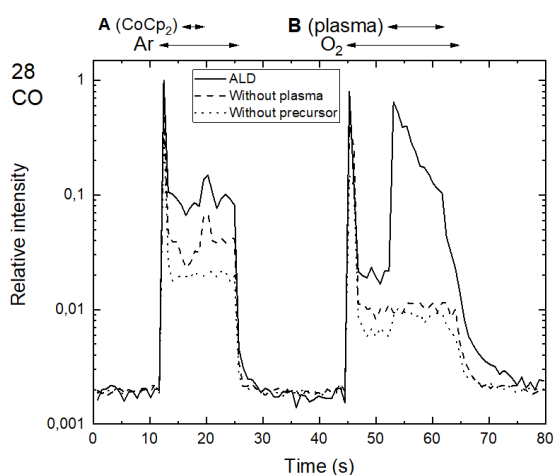


Figure 5.1: Time-resolved, normalized QMS measurement results of step A and B of recipe 1. $m/z=28$.

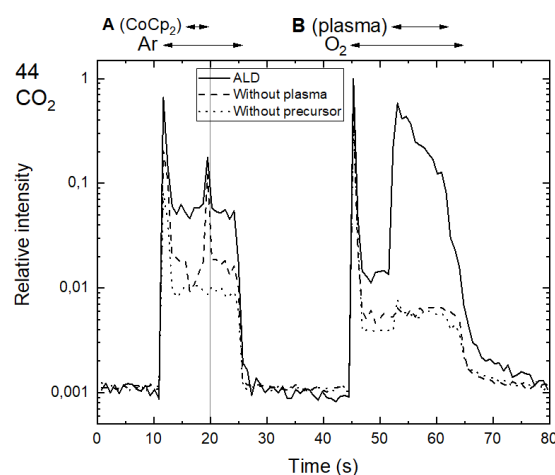


Figure 5.2: Time-resolved, normalized QMS measurement results of step A and B of recipe 1. $m/z=44$.

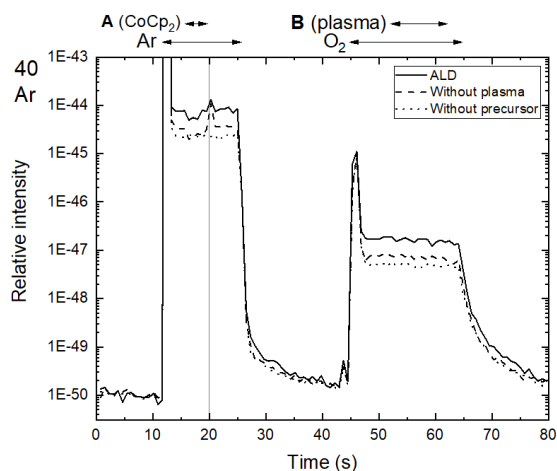


Figure 5.3: Time-resolved, normalized QMS measurement results of step A and B of recipe 1. $m/z=40$.

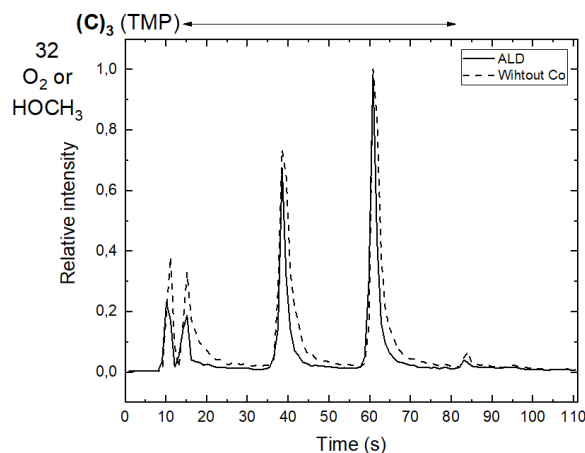


Figure 5.4: Time-resolved, normalized QMS measurement results of step C of recipe 2. $m/z=32$.

5.2 TMP reactions

5.2.1 Surface adsorption of TMP

As mentioned in section 4.1, the main peaks during TMP dosing are expected around mass 79 and 95. The measurements from these masses during the triple dosing of recipe 2 can be seen in Figure 5.5 and 5.6 respectively. The peaks of the full ALD cycle start off lower than the peaks of the cycle without Co. Each next cycle the top of the peak of the full ALD cycle gets closer to the top of the peak of the cycle without Co. This is expected, as during the cycle without Co the substrate cannot grow and therefore more TMP is able to reach the QMA, creating a higher signal. During the full ALD cycle, some of the TMP adsorbs to the surface of the substrate, and possibly also to the walls of the reactor, meaning less TMP reaches the QMA, creating a lower signal. After each cycle, the surface is more saturated and less TMP can adsorb to the surface, creating a signal closer to the one of the cycle without Co. As is visible from Figure 5.5 and 5.6, the surface is almost saturated after the third cycle.

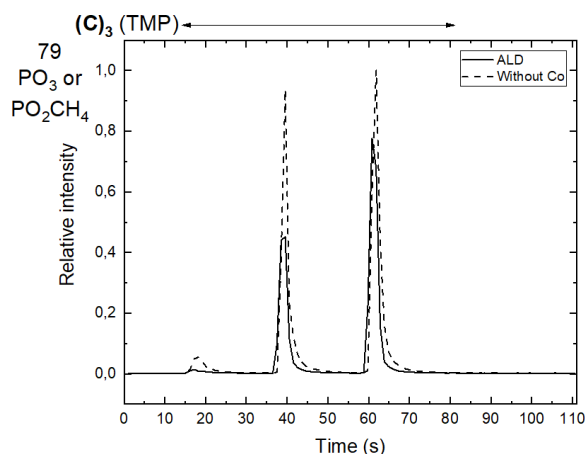


Figure 5.5: Time-resolved, normalized QMS measurement results of step C of recipe 2. $m/z=79$.

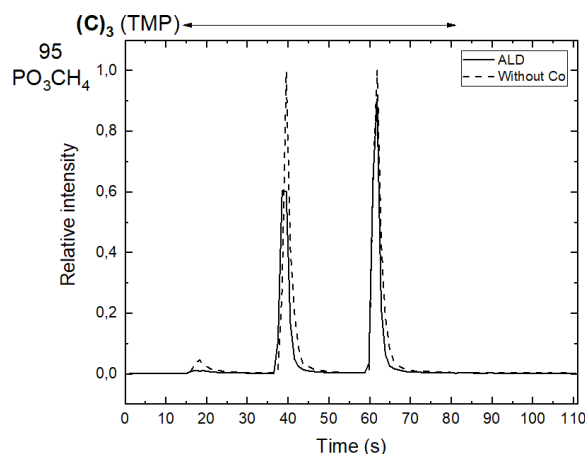


Figure 5.6: Time-resolved, normalized QMS measurement results of step C of recipe 2. $m/z=95$.

5.2.2 Reaction mechanisms of TMP

Mitchell et al.[48] proposed a possible reaction mechanism for the adsorption of dimethyl methylphosphonate (DMMP) on a metal oxide surface. DMMP is an organic molecule like TMP, which is similar in structure to TMP. The mechanisms can also be assumed to be similar, as the ligands of DMMP that are most reactive are the same as the ligands of TMP. The mechanism proposed by Mitchell et al.[48] is shown in Figure 5.7. For this reaction to happen, adsorbed hydroxyl (OH) groups have to be present on the surface. If this is the reaction happening at the surface, an increase in signal from methanol during the dosing of TMP is expected. In Figure 5.4 the measurement results of mass 32 (methanol and O₂) during the TMP dosing of the second recipe can be seen. The peaks of this mass during the full ALD cycle are just as high as the peaks of this mass during the cycle without Co. This means no distinguishable amount of methanol is being produced during this dosing step.

There are several possible reasons for these results. One possible reason is a lack of adsorbed hydroxyl or oxygen groups, meaning this specific reaction mechanism would be unable to take place. Another reason could be that oxygen is left over from the previous oxygen plasma step. This leftover oxygen could overshadow the relatively low amount of methanol. Due to the lack of signal from methanol, the proposed reaction mechanism cannot be confirmed.

A double peak at the beginning of Figure 5.4 is also visible. The first peak originates from before the first dosing of TMP. As this double peak is not visible for other masses during recipe 2, which can be seen in Figure 5.5 and 5.6, something mass related is happening. As mentioned in section 4.2, the valve to the QMA during recipe 2 is closed for most of the ALD cycle, and only opened during the dosing of TMP. This means a few seconds before the first dosing of TMP, the valve to the QMA is opened. Opening of the valve can cause a sudden pressure increase in the QMA. Leftover oxygen from the previous step together with the pressure increase could explain the first peak in Figure 5.4. This would also be in line the lack of signal from methanol, as the leftover oxygen could overshadow its signal during the dosing of TMP.

To be able to either in- or exclude the reaction mechanism proposed by Mitchell et al.[48], future QMS measurements can be done of not only methanol, but also of its fragmentation products like OCH₃, CH₃, and CH₂. These masses do not overlap with other ions that are present in the reaction chamber, giving better insight into the created byproducts.

Another possible reaction mechanism is proposed by Yong-Xi Li et al.[50] and is shown in Figure 5.8. For this reaction adsorbed oxygen needs to be present on the surface, and it would result in the release of formic acid (HCOOH), which has a mass of 46. This mass was not followed and therefore no conclusions about this reaction can be drawn. To also either in- or exclude this reaction mechanism in the future, mass 46 of formic acid can be followed.

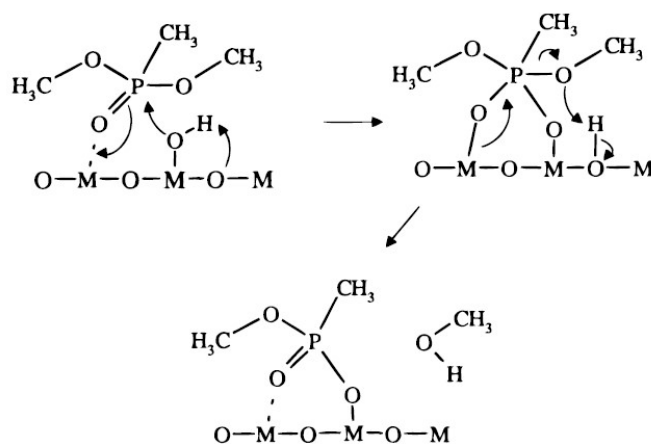


Figure 5.7: First reaction mechanism of TMP on a metal oxide surface[48].

5.2.3 Burning of the ligands of TMP

Step B and D of recipe 1 for mass 29 and 30 can be seen in Figure 5.10 and 5.11 respectively. A steep rise in signal from both masses is visible during the full ALD cycle, indicating a combustion reaction is taking place during

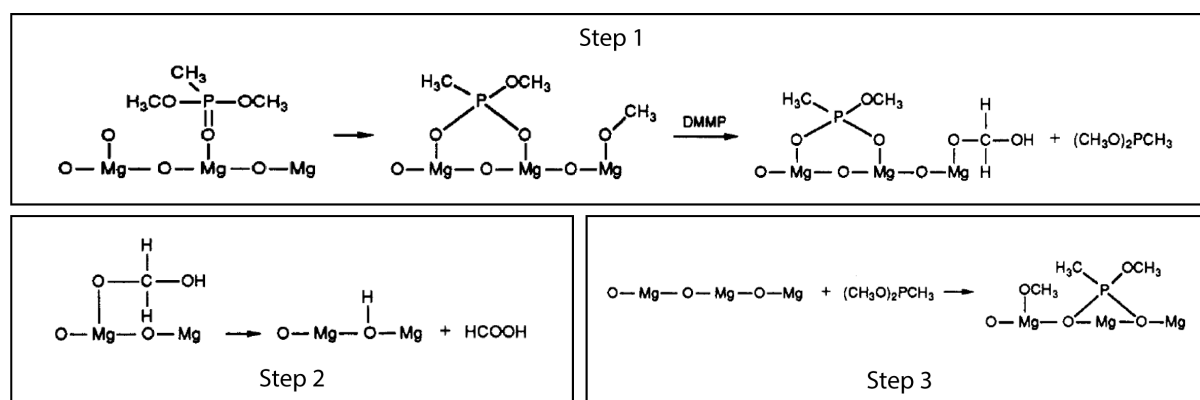


Figure 5.8: Second reaction mechanism of TMP on a metal oxide surface[50].

this step. This is in line with results from Y. Bai et al.[51], who researched the degradation of dichlorvos under the influence of an oxygen plasma. The degradation pattern proposed by Y. Bai et al.[51], presented in Figure 5.9, shows TMP first fragmenting into $\text{O}(\text{OCH}_3)_2\text{PH}$ and OCH_2 . Then, after longer exposure to the oxygen plasma, only PO_4^{3-} , CO_2 , and H_2O are left. If the ligands are burned in the same way as proposed here, production of OCH_2 ($m/z=29$) is expected. The measurement results of step B and D of recipe 1 for OCH_2 and OCH are shown in Figure 5.12 and 5.13 respectively. An increase in signal can be seen for both molecules when the plasma is turned on, making it likely that the reaction mechanism suggested by Y. Bai et al.[51] is taking place when the oxygen plasma is turned on.

A possible method that can be used in the future to check these results is to run the same recipes again, now using Fourier transformed infrared spectroscopy (FTIR) to measure the molecules that are present in the reaction chamber. FTIR uses the absorption and emission properties of a solid, liquid, or gas, to obtain an infrared spectrum[52]. From this infrared spectrum, the composition of e.g. a gas can be found. Because this measurement uses a different property of the gas to measure its composition than QMS, it can be used to independently confirm or reject the conclusions drawn from these QMS measurements.

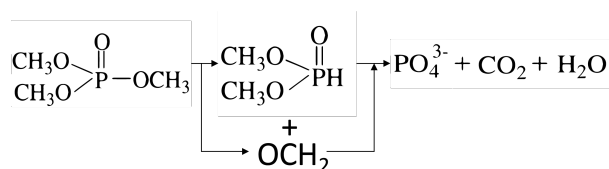


Figure 5.9: Reaction mechanism for the burning of ligands of TMP[51].

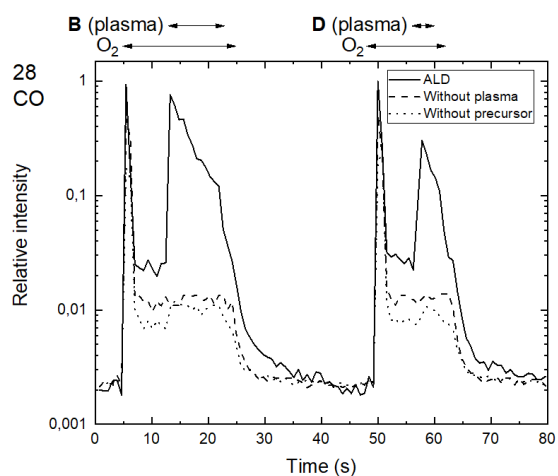


Figure 5.10: Time-resolved, normalized QMS measurement results of step B and D of recipe 1. $m/z=28$.

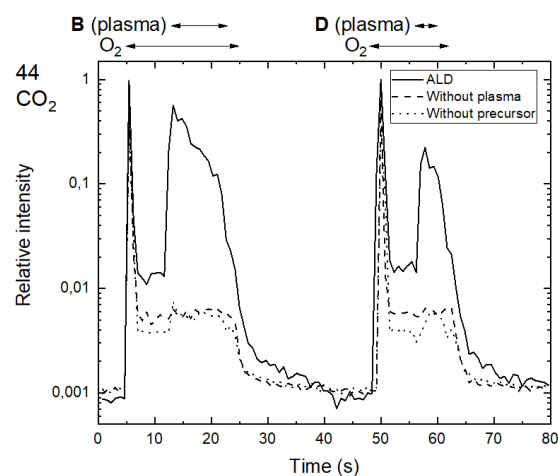


Figure 5.11: Time-resolved, normalized QMS measurement results of step B and D of recipe 1. $m/z=44$.

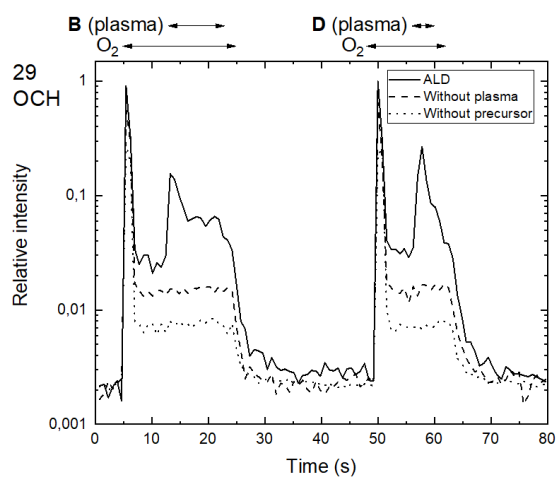


Figure 5.12: Time-resolved, normalized QMS measurement results of step B and D of recipe 1. $m/z=29$.

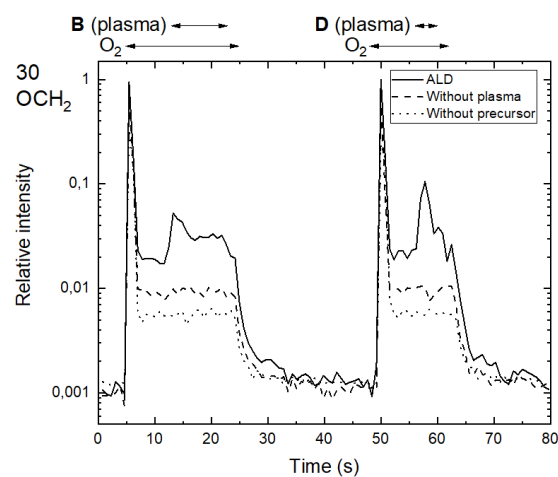


Figure 5.13: Time-resolved, normalized QMS measurement results of step B and D of recipe 1. $m/z=30$.

6 Conclusion

A rise in signal from mass 28 and 44 is observed during both step B and D of the first recipe. This rise can be attributed to a combustion reaction happening when the oxygen plasma is turned on. The measured combustion reaction during step B is in agreement with measurements from M.E. Donders et al.[49] on Co_3O_4 deposition. A rise in signal from masses 29 and 44 is also observed during step D of the first recipe. This can be linked to intermediate products from the combustion reaction happening during this step. The combustion reaction happening during step D, together with the creation of these intermediate products, is in agreement with measurements from Y. Bai et al.[51].

The increase in signal from mass 44 during step A of the first recipe can be attributed to a pressure increase caused by switching of the Ar flow from the bubbler, to going directly into the reaction chamber. This theory is further strengthened by the same increase happening in the signal from Ar, which should be non-reactive.

TMP is observed to be adsorbing to the surface during step C of the second recipe, visible from the first and second peak in mass 79 and 95 during the full ALD cycle being lower than these peaks in the cycle without Co. After the third dosing the surface is saturated, as the signal from the full ALD cycle is just as high as the signal from the cycle without Co.

No conclusions can be drawn regarding the two reaction mechanisms proposed in section 5.2. The intensity of the signal from mass 32 observed during step C of recipe 2 is the same for both the full ALD cycle and the cycle without Co. The double peak for mass 32 at the beginning of step C of recipe 2 can be attributed to the opening of the valve to the QMA, resulting in a pressure spike. Leftover oxygen from the previous step, together with this pressure increase, results in the initial peak before the first dosing of TMP.

7 Acknowledgments

This project would not have been possible without the help of some people, for which I am ever so grateful.

First of all, I want to thank my main supervisor M. Creatore for making this project possible.

I also want to thank my daily supervisor V. Di Palma for guiding me through this project. His advice helped me greatly and I have learned a lot the last few months.

Also, thanks to everyone of the Plasma & Materials Processing group who enabled me to do this project and helped me with it along the way.

Then lastly, I want to thank my roommates for giving me advice without complaining and providing me with a healthy dose of distraction.

References

- [1] IEA. International energy outlook 2017. [https://www.eia.gov/outlooks/ieo/pdf/0484\(2017\).pdf](https://www.eia.gov/outlooks/ieo/pdf/0484(2017).pdf), September 2017. Accessed: 2019-01-05.
- [2] ESA. Hydrogen energy storage. <http://energystorage.org/energy-storage/technologies/hydrogen-energy-storage>, 2019. Accessed: 2019-01-19.
- [3] Office of Energy Efficiency & Renewable Energy. Hydrogen storage. <https://www.energy.gov/eere/fuelcells/hydrogen-storage>, n.d.. Accessed: 2019-01-05.
- [4] epec. Battery cell comparison. <https://www.epectec.com/batteries/cell-comparison.html>, 2018. Accessed: 2019-01-05.
- [5] Office of Energy Efficiency & Renewable Energy. Hydrogen delivery. <https://www.energy.gov/eere/fuelcells/hydrogen-delivery>, n.d.. Accessed: 2019-01-05.
- [6] Office of Energy Efficiency & Renewable Energy. Hydrogen pipelines. <https://www.energy.gov/eere/fuelcells/hydrogen-pipelines>, n.d.. Accessed: 2019-01-05.
- [7] A Steinfeld. Solar hydrogen production via a two-step water-splitting thermochemical cycle based on zn/ZnO redox reactions. *International Journal of Hydrogen Energy*, 27(6):611–619, jun 2002. doi: 10.1016/s0360-3199(01)00177-x. URL [https://doi.org/10.1016/s0360-3199\(01\)00177-x](https://doi.org/10.1016/s0360-3199(01)00177-x).
- [8] C PERKINS. Likely near-term solar-thermal water splitting technologies. *International Journal of Hydrogen Energy*, 29(15):1587–1599, dec 2004. doi: 10.1016/j.ijhydene.2004.02.019. URL <https://doi.org/10.1016/j.ijhydene.2004.02.019>.
- [9] C. L. Muhich, B. W. Evanko, K. C. Weston, P. Lichty, X. Liang, J. Martinek, C. B. Musgrave, and A. W. Weimer. Efficient generation of h₂ by splitting water with an isothermal redox cycle. *Science*, 341(6145):540–542, aug 2013. doi: 10.1126/science.1239454. URL <https://doi.org/10.1126/science.1239454>.
- [10] Christopher L. Muhich, Brian D. Ehrhart, Ibraheam Al-Shankiti, Barbara J. Ward, Charles B. Musgrave, and Alan W. Weimer. A review and perspective of efficient hydrogen generation via solar thermal water splitting. *Wiley Interdisciplinary Reviews: Energy and Environment*, 5(3):261–287, may 2015. doi: 10.1002/wene.174. URL <https://doi.org/10.1002/wene.174>.
- [11] Stéphane Abanades and Gilles Flamant. Thermochemical hydrogen production from a two-step solar-driven water-splitting cycle based on cerium oxides. *Solar Energy*, 80(12):1611–1623, dec 2006. doi: 10.1016/j.solener.2005.12.005. URL <https://doi.org/10.1016/j.solener.2005.12.005>.
- [12] Xiumin Li, Xiaogang Hao, Abuliti Abudula, and Guoqing Guan. Nanostructured catalysts for electrochemical water splitting: current state and prospects. *Journal of Materials Chemistry A*, 4(31):11973–12000, 2016. doi: 10.1039/c6ta02334g. URL <https://doi.org/10.1039/c6ta02334g>.
- [13] Isabela C. Man, Hai-Yan Su, Federico Calle-Vallejo, Heine A. Hansen, José I. Martínez, Nilay G. Inoglu, John Kitchin, Thomas F. Jaramillo, Jens K. Nørskov, and Jan Rossmeisl. Universality in oxygen evolution electrocatalysis on oxide surfaces. *ChemCatChem*, 3(7):1159–1165, mar 2011. doi: 10.1002/cctc.201000397. URL <https://doi.org/10.1002/cctc.201000397>.
- [14] Peng Xiao, Wei Chen, and Xin Wang. A review of phosphide-based materials for electrocatalytic hydrogen evolution. *Advanced Energy Materials*, 5(24):1500985, oct 2015. doi: 10.1002/aenm.201500985. URL <https://doi.org/10.1002/aenm.201500985>.
- [15] Sengeni Anantharaj, Sivasankara Rao Ede, Kuppan Sakthikumar, Kannimuthu Karthick, Soumyaranjan Mishra, and Subrata Kundu. Recent trends and perspectives in electrochemical water splitting with an emphasis on sulfide, selenide, and phosphide catalysts of fe, co, and ni: A review. *ACS Catalysis*, 6(12):8069–8097, nov 2016. doi: 10.1021/acscatal.6b02479. URL <https://doi.org/10.1021/acscatal.6b02479>.
- [16] Jiahai Wang, Wei Cui, Qian Liu, Zhicai Xing, Abdullah M. Asiri, and Xuping Sun. Recent progress in cobalt-based heterogeneous catalysts for electrochemical water splitting. *Advanced Materials*, 28(2):215–230, nov 2015. doi: 10.1002/adma.201502696. URL <https://doi.org/10.1002/adma.201502696>.

- [17] Michal Bajdich, Mónica García-Mota, Aleksandra Vojvodic, Jens K. Nørskov, and Alexis T. Bell. Theoretical investigation of the activity of cobalt oxides for the electrochemical oxidation of water. *Journal of the American Chemical Society*, 135(36):13521–13530, aug 2013. doi: 10.1021/ja405997s. URL <https://doi.org/10.1021/ja405997s>.
- [18] Charles C. L. McCrory, Suho Jung, Ivonne M. Ferrer, Shawn M. Chatman, Jonas C. Peters, and Thomas F. Jaramillo. Benchmarking hydrogen evolving reaction and oxygen evolving reaction electrocatalysts for solar water splitting devices. *Journal of the American Chemical Society*, 137(13):4347–4357, mar 2015. doi: 10.1021/ja510442p. URL <https://doi.org/10.1021/ja510442p>.
- [19] InfoMine Inc. 5 year ruthenium prices and price charts. <http://www.infomine.com/investment/metal-prices/ruthenium/5-year/>, n.d.. Accessed: 2019-01-09.
- [20] InfoMine Inc. 5 year iridium prices and price charts. <http://www.infomine.com/investment/metal-prices/iridium/5-year/>, n.d.. Accessed: 2019-01-09.
- [21] Tingting Liu, Yanhui Liang, Qian Liu, Xuping Sun, Yuquan He, and Abdullah M. Asiri. Electrodeposition of cobalt-sulfide nanosheets film as an efficient electrocatalyst for oxygen evolution reaction. *Electrochemistry Communications*, 60:92–96, nov 2015. doi: 10.1016/j.elecom.2015.08.011. URL <https://doi.org/10.1016/j.elecom.2015.08.011>.
- [22] Pengzuo Chen, Kun Xu, Zhiwei Fang, Yun Tong, Junchi Wu, Xiuli Lu, Xu Peng, Hui Ding, Changzheng Wu, and Yi Xie. Metallic co₄n porous nanowire arrays activated by surface oxidation as electrocatalysts for the oxygen evolution reaction. *Angewandte Chemie*, 127(49):14923–14927, oct 2015. doi: 10.1002/ange.201506480. URL <https://doi.org/10.1002/ange.201506480>.
- [23] Lisi Xie, Rong Zhang, Liang Cui, Danni Liu, Shuai Hao, Yongjun Ma, Gu Du, Abdullah M. Asiri, and Xuping Sun. High-performance electrolytic oxygen evolution in neutral media catalyzed by a cobalt phosphate nanoarray. *Angewandte Chemie International Edition*, 56(4):1064–1068, dec 2016. doi: 10.1002/anie.201610776. URL <https://doi.org/10.1002/anie.201610776>.
- [24] V. Di Palma, G. Zafeiropoulos, T. Goldsweer, W.M.M. Kessels, M.C.M. van de Sanden, M. Creatore, and M.N. Tsampas. Atomic layer deposition of cobalt phosphate thin films for the oxygen evolution reaction. *Electrochemistry Communications*, 98:73–77, jan 2019. doi: 10.1016/j.elecom.2018.11.021. URL <https://doi.org/10.1016/j.elecom.2018.11.021>.
- [25] Steven M. George. Atomic layer deposition: An overview. *Chemical Reviews*, 110(1):111–131, jan 2010. doi: 10.1021/cr900056b. URL <https://doi.org/10.1021/cr900056b>.
- [26] H.C.M. Knoop, S.E. Potts, A.A. Bol, and W.M.M. Kessels. 27 - atomic layer deposition. In Thomas F. Kuech, editor, *Handbook of Crystal Growth (Second Edition)*, Handbook of Crystal Growth, pages 1101 – 1134. North-Holland, Boston, second edition, 2015. ISBN 978-0-444-63304-0. doi: <https://doi.org/10.1016/B978-0-444-63304-0.00027-5>. URL <http://www.sciencedirect.com/science/article/pii/B9780444633040000275>.
- [27] Markku Leskelä and Mikko Ritala. Atomic layer deposition (ALD): from precursors to thin film structures. *Thin Solid Films*, 409(1):138–146, apr 2002. doi: 10.1016/s0040-6090(02)00117-7. URL [https://doi.org/10.1016/s0040-6090\(02\)00117-7](https://doi.org/10.1016/s0040-6090(02)00117-7).
- [28] Jeffrey C Demmin. Special report-process technology update: Progress on all fronts-ultra-shallow junctions. *Solid State Technology*, 44(1):68–69, 2001.
- [29] Mikko Ritala and Markku Leskelä. Atomic layer epitaxy-a valuable tool for nanotechnology? *Nanotechnology*, 10(1):19, 1999.
- [30] Lauri Niinistö. Atomic layer epitaxy. *Current Opinion in Solid State and Materials Science*, 3(2):147–152, 1998.
- [31] S Haukka, E-L Lakomaa, and T Suntola. Adsorption controlled preparation of heterogeneous catalysts. In *Studies in Surface Science and Catalysis*, volume 120, pages 715–750. Elsevier, 1999.
- [32] Matthew W. Kanan, Yogesh Surendranath, and Daniel G. Nocera. Cobalt-phosphate oxygen-evolving compound. *Chem. Soc. Rev.*, 38(1):109–114, 2009. doi: 10.1039/b802885k. URL <https://doi.org/10.1039/b802885k>.

- [33] Yogesh Surendranath, Mircea Dincă, and Daniel G. Nocera. Electrolyte-dependent electrosynthesis and activity of cobalt-based water oxidation catalysts. *Journal of the American Chemical Society*, 131(7):2615–2620, feb 2009. doi: 10.1021/ja807769r. URL <https://doi.org/10.1021/ja807769r>.
- [34] Eindhoven University of Technology. Illustrations atomic layer etching (alet) process. <http://www.nanomanufacturing.nl/ALE/>, n.d. Accessed: 2019-01-16.
- [35] Riikka L. Puurunen. Surface chemistry of atomic layer deposition: A case study for the trimethylaluminum/water process. *Journal of Applied Physics*, 97(12):121301, jun 2005. doi: 10.1063/1.1940727. URL <https://doi.org/10.1063/1.1940727>.
- [36] Hyungjun Kim and Il-Kwon Oh. Review of plasma-enhanced atomic layer deposition: Technical enabler of nanoscale device fabrication. *Japanese Journal of Applied Physics*, 53(3S2):03DA01, jan 2014. doi: 10.7567/jjap.53.03da01. URL <https://doi.org/10.7567/jjap.53.03da01>.
- [37] Philip E. Miller and M. Bonner Denton. The quadrupole mass filter: Basic operating concepts. *Journal of Chemical Education*, 63(7):617, jul 1986. doi: 10.1021/ed063p617. URL <https://doi.org/10.1021/ed063p617>.
- [38] Brian M. Tissue. Quadrupole mass spectrometry. <https://www.tissuegroup.chem.vt.edu/chem-ed/ms/quadrupo.html>, 2000. Accessed: 2019-02-07.
- [39] Peter H Dawson. *Quadrupole mass spectrometry and its applications*. Elsevier, 2013.
- [40] B. A. Thomson and J. R. Roberts. A new technique for the rapid analysis of soil for the presence of polychlorinated biphenyls. *International Journal of Environmental Analytical Chemistry*, 11(2):139–151, apr 1982. doi: 10.1080/03067318208078306. URL <https://doi.org/10.1080/03067318208078306>.
- [41] Y. Hajar, V. Di Palma, V. Kyriakou, M.A. Verheijen, E.A. Baranova, P. Vernoux, W.M.M. Kessels, M. Creatore, M.C.M. van de Sanden, and M.N. Tsampas. Atomic layer deposition of highly dispersed pt nanoparticles on a high surface area electrode backbone for electrochemical promotion of catalysis. *Electrochemistry Communications*, 84:40–44, nov 2017. doi: 10.1016/j.elecom.2017.09.023. URL <https://doi.org/10.1016/j.elecom.2017.09.023>.
- [42] H. C. M. Knoop, A. J. M. Mackus, M. E. Donders, M. C. M. van de Sanden, P. H. L. Notten, and W. M. M. Kessels. Remote plasma ALD of platinum and platinum oxide films. *Electrochemical and Solid-State Letters*, 12(7):G34, 2009. doi: 10.1149/1.3125876. URL <https://doi.org/10.1149/1.3125876>.
- [43] S. B. S. Heil, E. Langereis, F. Roozeboom, M. C. M. van de Sanden, and W. M. M. Kessels. Low-temperature deposition of TiN by plasma-assisted atomic layer deposition. *Journal of The Electrochemical Society*, 153(11):G956, 2006. doi: 10.1149/1.2344843. URL <https://doi.org/10.1149/1.2344843>.
- [44] T. Goldsweeer. *Atomic layer deposition of cobalt phosphate thin films for the oxygen evolution reaction*. PhD thesis, Eindhoven University of Technology, November 2018. unpublished thesis.
- [45] Donald A. Bafus, Emilio J. Gallegos, and Robert W. Kiser. An electron impact investigation of some alkyl phosphate esters. *The Journal of Physical Chemistry*, 70(8):2614–2619, aug 1966. doi: 10.1021/j100880a029. URL <https://doi.org/10.1021/j100880a029>.
- [46] Daniel Z. Brunengraber, Brendan J. McCabe, Jill Katanik, and Stephen F. Previs. Gas chromatography–mass spectrometry assay of the 18o enrichment of water as trimethyl phosphate. *Analytical Biochemistry*, 306(2):278–282, jul 2002. doi: 10.1006/abio.2002.5720. URL <https://doi.org/10.1006/abio.2002.5720>.
- [47] AIST. Spectral database for organic compounds sdb. https://sdb.db.aist.go.jp/sdb/cgi-bin/direct_frame_top.cgi, March 1999. Accessed: 2019-01-20.
- [48] Mark B. Mitchell, V. N. Sheinker, and Eric A. Mintz. Adsorption and decomposition of dimethyl methylphosphonate on metal oxides. *The Journal of Physical Chemistry B*, 101(51):11192–11203, dec 1997. doi: 10.1021/jp972724b. URL <https://doi.org/10.1021/jp972724b>.
- [49] M. E. Donders, H. C. M. Knoop, M. C. M. van, W. M. M. Kessels, and P. H. L. Notten. Remote plasma atomic layer deposition of co₃o₄ thin films. *Journal of The Electrochemical Society*, 158(4):G92, 2011. doi: 10.1149/1.3552616. URL <https://doi.org/10.1149/1.3552616>.

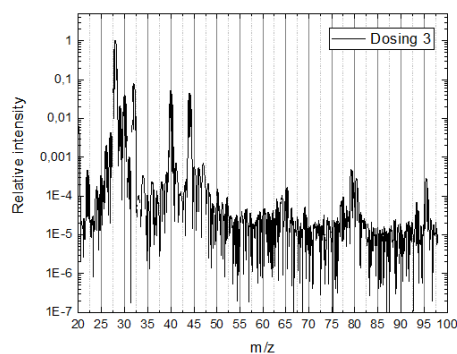
- [50] Yong Xi Li, Olga Koper, Maher Atteya, and Kenneth J Klabunde. Adsorption and decomposition of organophosphorus compounds on nanoscale metal oxide particles. in situ gc-ms studies of pulsed microreactions over magnesium oxide. *Chemistry of materials*, 4(2):323–330, 1992.
- [51] Yanhong Bai, Jierong Chen, Yun Yang, Limei Guo, and Chunhong Zhang. Degradation of organophosphorus pesticide induced by oxygen plasma: Effects of operating parameters and reaction mechanisms. *Chemosphere*, 81(3):408–414, sep 2010. doi: 10.1016/j.chemosphere.2010.06.071. URL <https://doi.org/10.1016/j.chemosphere.2010.06.071>.
- [52] Peter Griffiths. *Fourier transform infrared spectrometry*. Wiley-Interscience, Hoboken, NJ, 2007. ISBN 978-0-471-19404-0.

Appendices

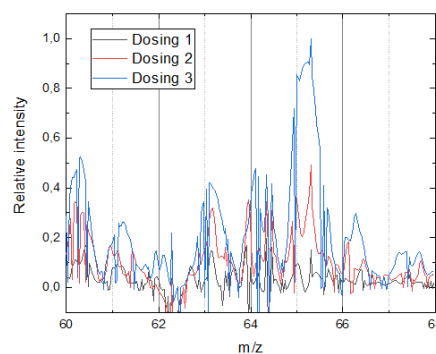
Appendix A Preliminary Testing Figures

m/e	RA ^a at 70 v	—AP, ev—	Probable process
15	100.0	18.6 ± 0.3	$C_3H_9O_4P \rightarrow CH_3^+ + ?$
29	36.6	17.3 ± 0.4	$\rightarrow CHO^+ + ?$
31	16.7	17.3 ± 0.4	$\rightarrow CH_3O^+ + ?$
45	1.3	14.0 ± 0.2	$\rightarrow C_2H_5O^+ + ?$
47	22.0	19.6 ± 0.3	$\rightarrow PO^+ + 2CH_2O + CH_3O + 2H$
48	2.0		$\rightarrow HPO^+ + H + 2CH_2O + CH_3O$
65	5.0	15.1 ± 0.3	$\rightarrow H_2O_2P^+ + 2CH_2O + CH_3$
79	26.6	15.1 ± 0.2	$\rightarrow CH_4O_2P^+ + 2CH_2O + H$
80	17.3	13.9 ± 0.4	$\rightarrow CH_3O_2P^+ + 2CH_2O$
95	22.1	14.4 ± 0.3	$\rightarrow CH_4O_3P^+ + CH_2O + CH_3$
109	28.0	$(14.3)^b$	$\rightarrow C_2H_4O_2P^+ + CH_2O + H$
110	86.3	11.9 ± 0.2	$\rightarrow C_2H_7O_3P^+ + CH_2O$
139	5.4		$\rightarrow C_3H_5O_4P^+ + H$
140	14.0	10.77 ± 0.30^b	$\rightarrow C_3H_5O_4P^+$

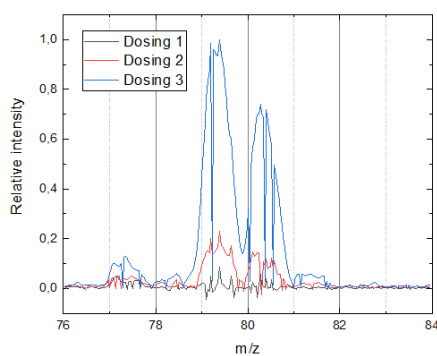
Figure A.1: Mass spectrum of TMP and the possible principal positive ions belonging to each m/z value.[45]



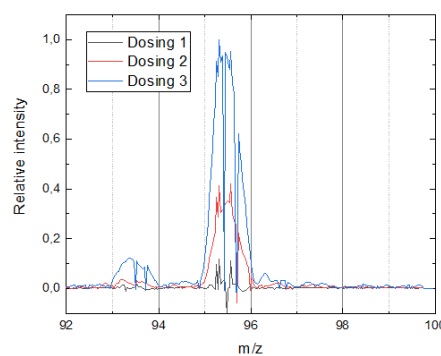
(a) Logarithmic plot with an m/z from 20-100.



(b) Linear plot with an m/z from 60-68.



(c) Linear plot with an m/z from 76-84.



(d) Linear plot with an m/z from 92-100.

Figure A.2: Plots of the electron impact ionization spectrum of TMP for different ranges.

Declaration concerning the TU/e Code of Scientific Conduct for the Bachelor's final project

I have read the TU/e Code of Scientific Conductⁱ.

I hereby declare that my Bachelor's final project has been carried out in accordance with the rules of the TU/e Code of Scientific Conduct

Date

21-02-2019

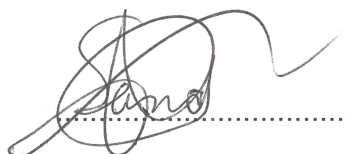
Name

S.H.L. Raaijmakers

ID-number

0958930

Signature



Submit the signed declaration to the student administration of your department.

ⁱ See: <http://www.tue.nl/en/university/about-the-university/integrity/scientific-integrity/>

The Netherlands Code of Conduct for Academic Practice of the VSNU can be found here also.

More information about scientific integrity is published on the websites of TU/e and VSNU